

# Atomic Structure and Spectroscopy of Single Metal (Cr, V) Substitutional Dopants in Monolayer MoS<sub>2</sub>

Alex W. Robertson,<sup>\*,†</sup> Yung-Chang Lin,<sup>‡</sup> Shanshan Wang,<sup>†</sup> Hidetaka Sawada,<sup>†,§,||</sup> Christopher S. Allen,<sup>†,||</sup> Qu Chen,<sup>†</sup> Sungwoo Lee,<sup>⊥</sup> Gun-Do Lee,<sup>⊥</sup> Joohee Lee,<sup>⊥</sup> Seungwu Han,<sup>⊥</sup> Euijoon Yoon,<sup>⊥</sup> Angus I. Kirkland,<sup>†,||</sup> Heeyeon Kim,<sup>#</sup> Kazu Suenaga,<sup>‡</sup> and Jamie H. Warner<sup>\*,†</sup>

<sup>†</sup>Department of Materials, University of Oxford, Parks Road, Oxford OX1 3PH, United Kingdom

<sup>‡</sup>Nanotube Research Center, National Institute of Advanced Industrial Science and Technology (AIST), AIST Central 5, Tsukuba 305-8564, Japan

<sup>§</sup>JEOL Limited, 3-1-2 Musashino, Akishima, Tokyo 196-8558, Japan

<sup>||</sup>Electron Physical Sciences Imaging Center, Diamond Light Source Limited, Didcot, Oxfordshire OX11 0DE, United Kingdom

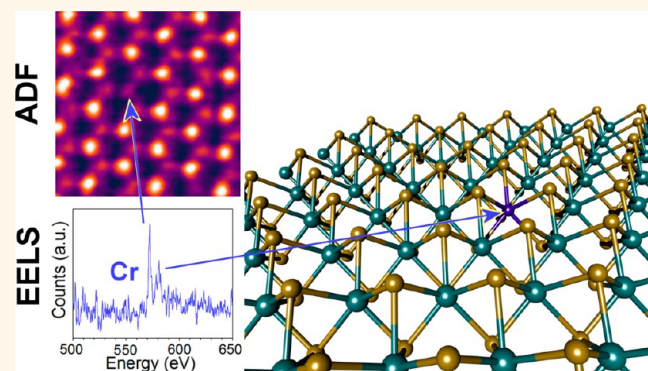
<sup>⊥</sup>Department of Materials Science and Engineering, Seoul National University, Seoul 151-742, Korea

<sup>#</sup>Convergence Materials Laboratory, Korea Institute of Energy Research, 152 Gajeong-ro, Yuseong-gu, Daejeon 305-343, Korea

## S Supporting Information

**ABSTRACT:** Dopants in two-dimensional dichalcogenides have a significant role in affecting electronic, mechanical, and interfacial properties. Controllable doping is desired for the intentional modification of such properties to enhance performance; however, unwanted defects and impurity dopants also have a detrimental impact, as often found for chemical vapor deposition (CVD) grown films. The reliable identification, and subsequent characterization, of dopants is therefore of significant importance. Here, we show that Cr and V impurity atoms are found in CVD grown MoS<sub>2</sub> monolayer 2D crystals as single atom substitutional dopants in place of Mo. We attribute these impurities to trace elements present in the MoO<sub>3</sub> CVD precursor. Simultaneous annular dark field scanning transmission electron microscopy (ADF-STEM) and electron energy loss spectroscopy (EELS) is used to map the location of metal atom substitutions of Cr and V in MoS<sub>2</sub> monolayers with single atom precision. The Cr and V are stable under electron irradiation at 60 to 80 kV, when incorporated into line defects, and when heated to elevated temperatures. The combined ADF-STEM and EELS differentiates these Cr and V dopants from other similar contrast defect structures, such as 2S self-interstitials at the Mo site, preventing misidentification. Density functional theory calculations reveal that the presence of Cr or V causes changes to the density of states, indicating doping of the MoS<sub>2</sub> material. These transferred impurities could help explain the presence of trapped charges in CVD prepared MoS<sub>2</sub>.

**KEYWORDS:** MoS<sub>2</sub>, STEM, electron microscopy, defects, TEM, dopants, EELS



The direct band gap monolayer MoS<sub>2</sub> is one of a family of layered metal dichalcogenides<sup>1</sup> that show promise in applications including catalysis, transistors, and optoelectronics.<sup>2–7</sup> Scalable synthesis of these materials is currently an active area of research, focusing primarily on either liquid exfoliation<sup>8,9</sup> or chemical vapor deposition (CVD) techniques.<sup>10–13</sup> However, impurities in the source material(s) are likely to have a significant role in the properties of any synthesized MoS<sub>2</sub>. The role of impurities and dopants are especially significant for these layered materials as not only do

they provide a means for tuning the carrier concentration and mobility,<sup>14–16</sup> but they also have implications for interface properties. This latter effect is due to monolayer materials essentially being “all-surface” structures, and thus, any lattice dopants will be part of a potential interface. The consequences

**Received:** August 23, 2016

**Accepted:** October 21, 2016

**Published:** November 7, 2016

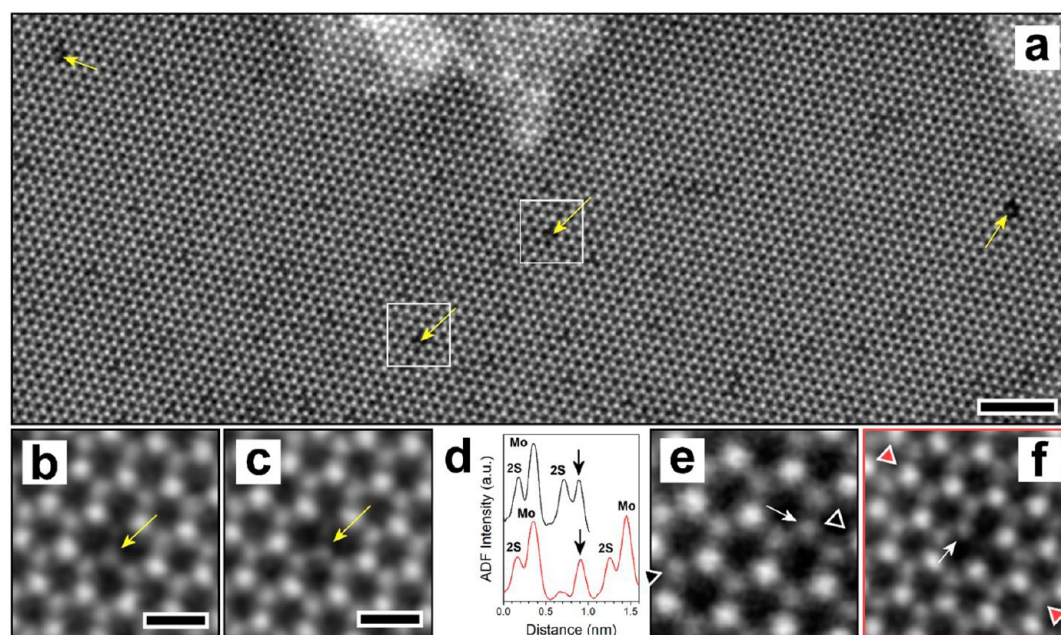


Figure 1. ADF-STEM characterization of CVD grown MoS<sub>2</sub> at room temperature. (a) Large area ADF-STEM image of monolayer MoS<sub>2</sub>. Low contrast intensities situated at Mo atomic sites are indicated with yellow arrows. Scale bar is 2 nm. (b,c) High magnification images of the left and right boxed areas in (a), respectively. Scale bars are 0.5 nm. (d) ADF intensity line profiles taken from the two dopant sites in (e) and (f). Dopant sites are indicated with arrows, and profiles were measured between the pointers shown. Beam accelerating voltage at 80 kV.

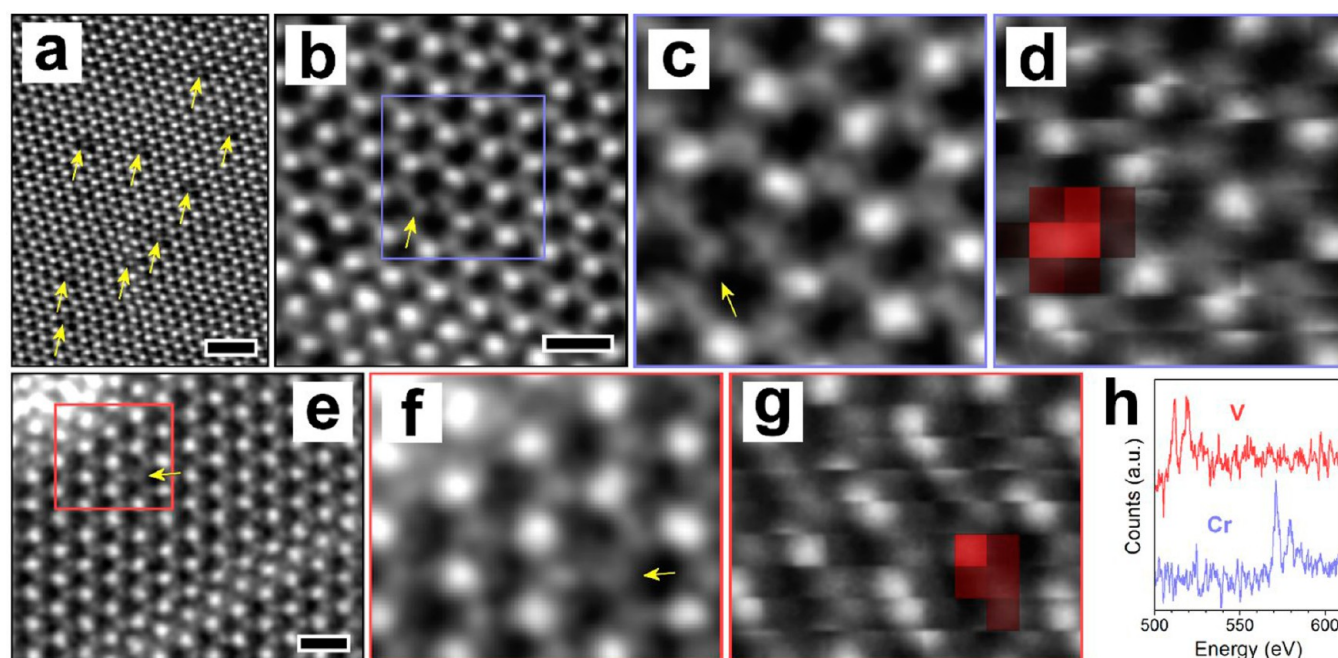
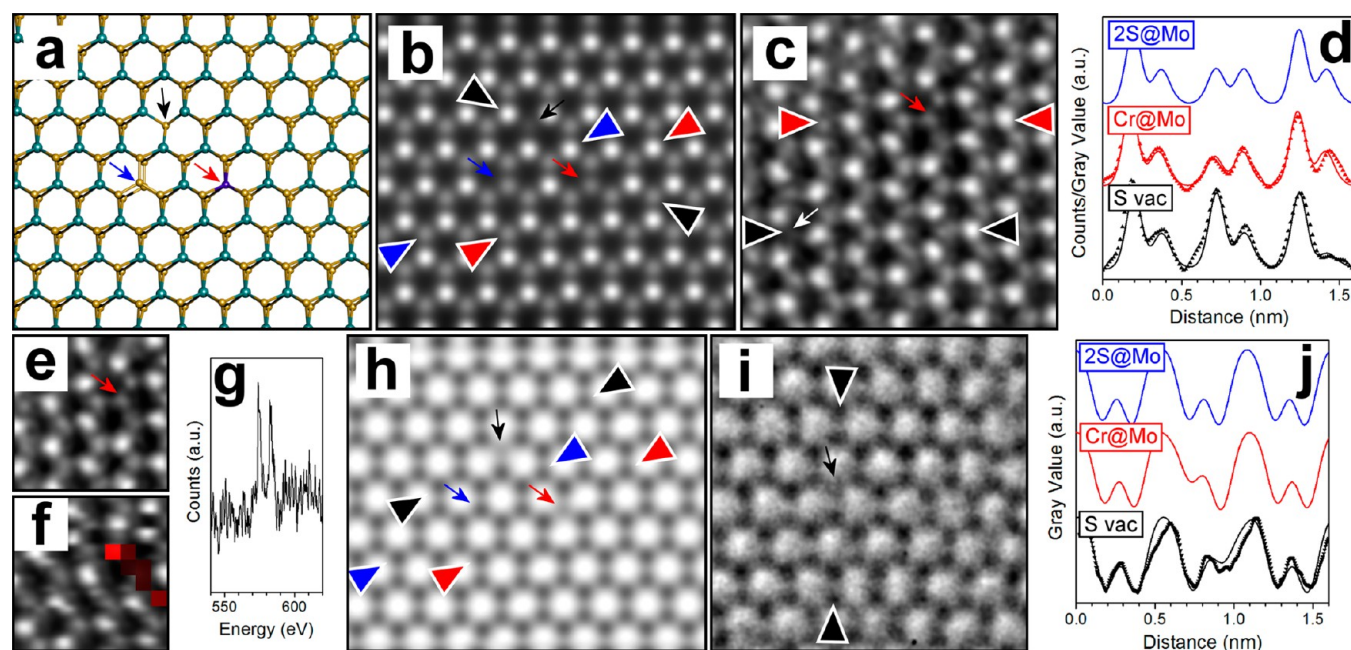


Figure 2. ADF-STEM with simultaneous EELS mapping of single atom Cr and V substitution sites (Cr@Mo and V@Mo). (a) ADF-STEM image of MoS<sub>2</sub> at 300 °C with low contrast single atoms situated at some Mo sites (arrows), in agreement with room temperature experiments. Scale bar corresponds to 1 nm. (b) ADF-STEM image indicating the region for EELS mapping. Scale bar corresponds to 0.5 nm. (c) Magnified ADF-STEM image from the region indicated with the box in (b). (d) Overlay of the integrated EELS intensity (between 570–590 eV) onto the ADF-STEM image acquired at the same time, showing a Cr@Mo substitution in the dopant region. Higher red intensity corresponds to greater integrated EELS intensity in the region 570–590 eV for the scanned pixel. (e) ADF-STEM image indicating the region for EELS mapping. Scale bar corresponds to 0.5 nm. (f) Magnified ADF-STEM image from the boxed region in (e). (g) Overlay of the integrated EELS intensity (between 505–525 eV) onto the ADF-STEM image acquired at the same time, showing a V@Mo substitution in the dopant region. (h) EELS spectra showing the Cr L<sub>3,2</sub> and V L<sub>3,2</sub> edges extracted from the EELS maps in (d) and (g), respectively. Beam accelerating voltage at 60 kV.

of this are important for heterostructures, low Schottky barrier metal contacts, and catalysis. Variability in device performance

for mechanically exfoliated MoS<sub>2</sub> has been experimentally observed as both large spatial variations in contact resistance<sup>17</sup>



**Figure 3.** Distinguishing Cr@Mo and 2S@Mo by Z contrast in ADF-STEM and AC-TEM. (a) Perspective view of the MoS<sub>2</sub> atomic model used for simulations, with an S vacancy (black arrow), Cr@Mo (red arrow), and 2S@Mo (blue arrow) indicated. (b) Simulated ADF image of the model in (a). (c) Experimental ADF-STEM image of MoS<sub>2</sub> (300 °C). White arrow indicates an S vacancy, red arrow a Cr@Mo. (d) Intensity line profiles between the respectively colored pointers in the simulated (line plot), and experimental (scatter plot) ADF images (b and c). (e) ADF-STEM image (300 °C) of a Cr dopant taken with simultaneous EELS map of the Cr@Mo shown in (c). (f) Overlap of EELS signal (570–590 eV) from EELS map onto the ADF-STEM image. (g) EELS signal from the dopant region. (h) Simulated TEM image of (a). (i) Experimental TEM image of MoS<sub>2</sub> (room temperature). Black arrow indicates an S vacancy. (j) Intensity line profiles taken between the appropriately colored pointers in the simulated (line plot), and experimental (scatter plot) TEM images (h and i). Beam accelerating voltage at 60 kV for ADF-STEM and 80 kV for TEM.

and as unexpected Ohmic contacts with high work function materials,<sup>14,18–21</sup> effects which have recently been attributed to intrinsic defects and impurities.<sup>22</sup> Further, the performance of CVD MoS<sub>2</sub>, grown using the common MoO<sub>3</sub> sulfurization technique, in electronic and optical devices has demonstrated some variability in the literature. This includes the reporting of the presence of defect induced charge trap states, reducing electronic device performance.<sup>23–26</sup>

The importance of understanding these dopants and impurities has motivated the exploration of atomic level defects and doping of MoS<sub>2</sub> using both theory<sup>27–29</sup> and experiment,<sup>30–35</sup> with the imaging of two-dimensional materials and the characterization of their associated structural defects developing into a significant area of research.<sup>36,37</sup> These experiments are valuable both for aiding the understanding of potential materials applications, ranging from optoelectronics<sup>38–40</sup> to water desalination,<sup>41,42</sup> and as model systems for understanding defect behavior in general.<sup>43–48</sup>

Aberration-corrected transmission electron microscopy (AC-TEM) and scanning TEM (AC-STEM) are essential techniques in this field due to their ability to image at the single atom level and to induce controlled defect formation in situ.<sup>49,50</sup> Utilizing annular dark-field (ADF) imaging in a STEM provides imaging intensities proportional to atomic number ( $Z^{1.4-2}$  contrast imaging), allowing for the straightforward discrimination of different element sites in two-dimensional materials.<sup>51–53</sup> This can be combined with electron energy loss spectroscopy (EELS) to confirm an elements identification.<sup>54,55</sup> This can allow the reliable imaging of single atom dopant structures, revealing the bonding configurations that dopants undergo,

such as substitutions<sup>27</sup> or surface bonded structures (e.g., top or bridge sites).<sup>28</sup>

In this work, we demonstrate that the definitive elemental identification of single atom Cr and V metal substitutions in MoS<sub>2</sub> monolayers achieved through the combination of both ADF-STEM imaging and EELS spatial mapping. We perform this investigation on our CVD-synthesized MoS<sub>2</sub> monolayers,<sup>56</sup> and find that Cr and V substitutions exist throughout. ADF-STEM imaging and single-atom EELS mapping are employed to confirm Cr and V atoms may occupy the Mo site as substitutional dopants. We show that the Cr and V atoms exhibit similar ADF contrast to two sulfurs and demonstrate the utility of EELS mapping to ensure correct elemental identification. We use the combination of ADF-STEM imaging and EELS mapping to characterize the stability of these dopants to elevated temperature and during defect formation.

## RESULTS AND DISCUSSION

ADF-STEM imaging of the CVD prepared monolayer MoS<sub>2</sub> (Figure 1a) revealed a significant concentration ( $\sim 0.01$ – $0.1$  atoms nm<sup>-2</sup>) of low contrast atoms situated on the Mo site spread across the sample (Figure 1b,c). These are distinct from low contrast features located on the S site, which can be attributed to S vacancy formation under electron beam irradiation (80 kV accelerating voltage). ADF intensity line profiles across these low contrast defect sites (Figure 1d) show an intensity comparable to that of 2 S atoms, which would intuitively suggest that these defects are 2S self-interstitials but does not discount them being a heavier atomic element.

To confirm the identity of the dopant elements we recorded atomic resolution EELS maps with simultaneous ADF-STEM

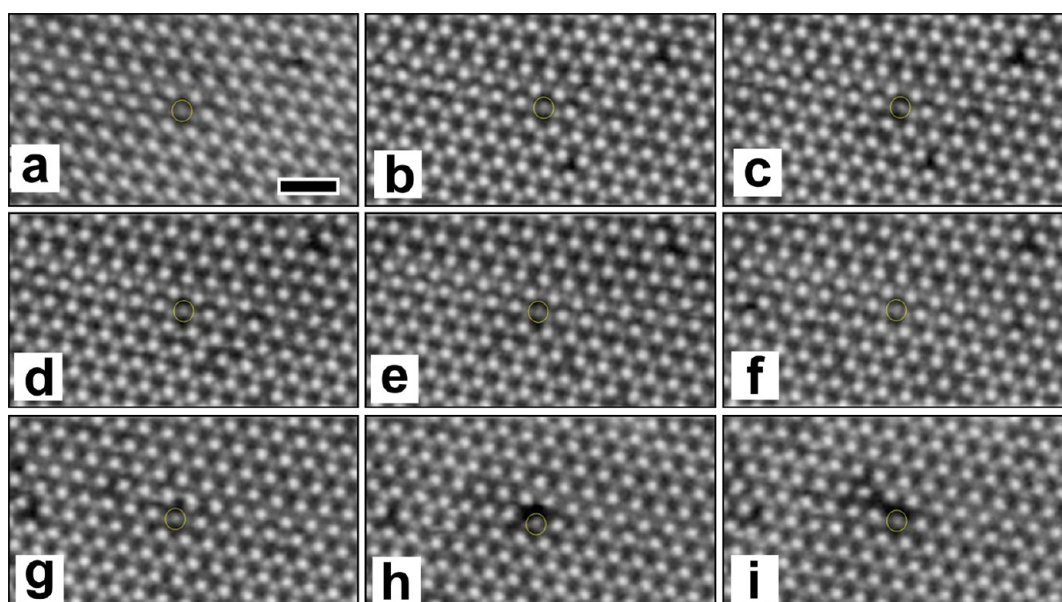


**Figure 4.** Room temperature stability of substitutional metal atom. Time series of ADF-STEM images at room temperature of a substitutional metal atom at the Mo site ( $t = 0$  s, 1 min 16 s, 1 min 40 s, 2 min 18 s, 2 min 43 s, 3 min 16 s, 4 min 35 s, 5 min 03 s, and 5 min 35 s, respectively). Beam accelerating voltage at 80 kV. Scale bar corresponds to 1 nm.

imaging of the MoS<sub>2</sub> monolayer. For these experiments, the sample was heated *in situ* to 300 °C in order to prevent contamination build-up during the relatively long simultaneous ADF-STEM imaging and EELS mapping acquisitions. A lower accelerating voltage of 60 kV was employed to minimize beam damage. Both Figure 1a and Figure 2a show similar defect configurations and distributions at room and elevated temperatures, suggesting that heating does not influence the presence or distribution of the substitutions. ADF-STEM imaging with atomic level EELS mapping revealed these low contrast defects to be single atom substitutions of Cr (38/43 instances, Figure 2b–d), or V (5/43 instances, Figure 2e–g), denoted Cr@Mo and V@Mo after refs 30, 58, and 59. Evidence for other metal adatom configurations, such as Cr+S@2S or Cr+Mo@Mo, was not found. The EELS mapping agrees with the ADF-STEM images, where Cr ( $Z = 24$ ) shows lower contrast than Mo ( $Z = 42$ ). The similarity in atomic number between V ( $Z = 23$ ) and Cr, and thus the similarity in contrast, emphasizes the value of EELS identification as a complement to ADF-STEM imaging.

We note that the ADF-STEM images of Cr@Mo give similar contrast to images of 2S self-interstitials on the Mo site, 2S@Mo, recently reported in the literature of ADF-STEM investigations of MoS<sub>2</sub>.<sup>31,33</sup> We have performed image simulations of Cr@Mo and 2S@Mo in monolayer MoS<sub>2</sub>, as well as for a single S vacancy to provide a known reference. A render of the input atomic model (perspective view) for these simulations is shown in Figure 3a, with the three defects indicated with arrows. ADF intensity line profiles of these three defects were acquired from the ADF image simulation (Figure 3b) and were compared with line profiles extracted from an experimental ADF image (Figure 3c), as shown in Figure 3d. The experimental ADF image in Figure 3c shows both a Cr@Mo substitution (red arrow), as confirmed by ADF-STEM imaging with simultaneous EELS mapping (Figure 3e–g), and an S vacancy (white arrow). The calculated and experimentally measured S vacancy intensity profiles (Figure 3d black line and scatter plots, respectively) were used to calibrate the relative contrast and brightness between the two, as well as to verify the

simulation parameters (see methods). This allows us to compare the simulated and experimentally measured ADF profiles for Cr@Mo and also to compare with the simulated 2S@Mo. From Figure 3d, it can be seen that the experimentally measured ADF profile of Cr@Mo (red scatter plot) agrees strongly with the simulated Cr@Mo profile (red line plot). However, there is also a close match between the Cr@Mo profile and the 2S@Mo simulation (blue line plot), although the Cr does exhibit marginally lower intensity than the 2S due to the lower  $Z$  ( $Z = 24$  vs  $Z = 16 \times 2 = 32$ ). This marginal difference can be observed in the experimental intensity profile, with the lower intensity for Cr compared to 2S in good agreement with the predicted simulation. The combination of EELS and ADF agreement allow us to be confident of the chemical identity of the substitution. However, the similar intensities of Cr@Mo and 2S@Mo in the ADF images demonstrates that intensity profile analysis from ADF-STEM imaging alone has the potential for ambiguity and in isolation could lead to misidentification of dopant and defect structures.

Our CVD grown monolayer MoS<sub>2</sub> has been characterized in previous work by AC-TEM;<sup>59</sup> however, no evidence of Cr dopants was detected. We attribute this to the lower sensitivity of phase contrast high resolution TEM imaging to small differences in atomic number, making the identification of defect and dopant sites more ambiguous to element composition. This is demonstrated in Figure 3h–j. A TEM image simulation of the model shown in Figure 3a is shown in Figure 3h, with an experimental TEM image shown in Figure 3i. Single S vacancies can be reliably identified using TEM from a combination of their weak contrast and that they are continually created during imaging at 80 kV accelerating voltage.<sup>57</sup> An S vacancy is identified in Figure 3i and used as calibration for the image simulation parameters and brightness/contrast, demonstrating good agreement with the intensity line profile shown in Figure 3j. From the intensity profiles we see that in AC-TEM a Cr@Mo site has comparable intensity to an S vacancy, so would appear indistinguishable from an S@Mo antisite. Although such features are apparent in our

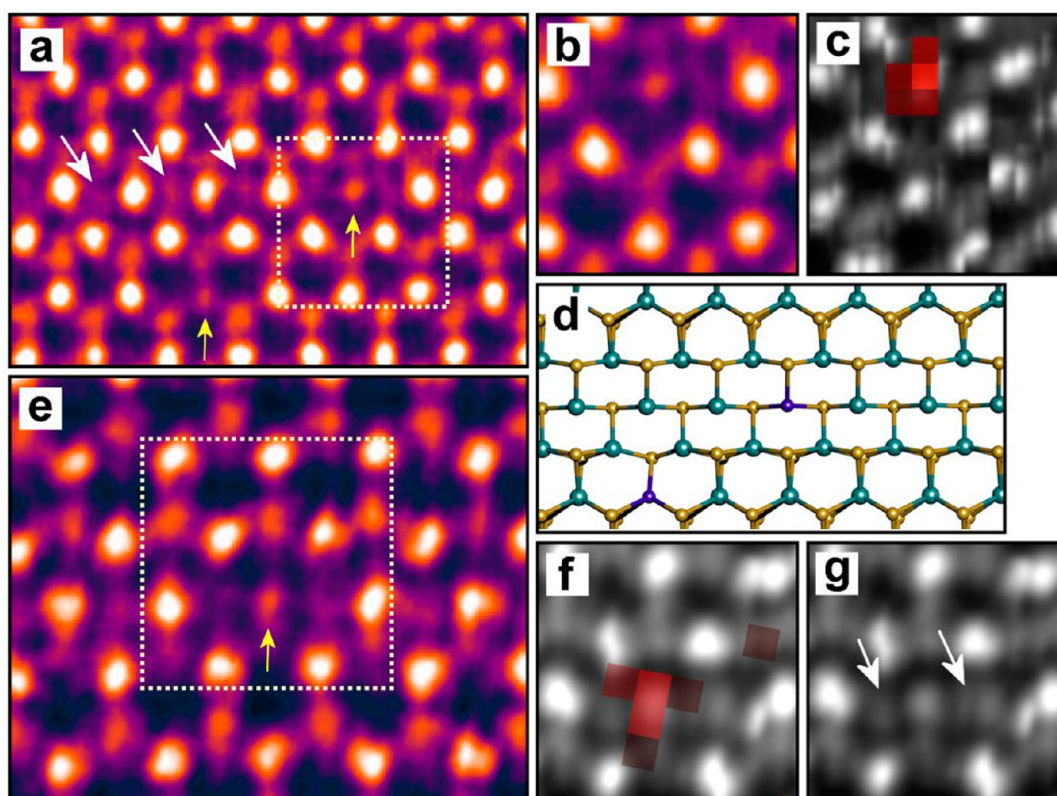


**Figure 5.** Inclusion of Cr substitutions in S vacancy line (SVL) defects. (a) ADF-STEM image of a 2SVL defect, with both a Cr@Mo in the bulk lattice and one imbedded in the line center (yellow arrows). White arrows indicate single S atoms within the SVL. (b) ADF-STEM image and (c) EELS map (570–590 eV) of the boxed region in (a). (d) Atomic model of (a). (e) ADF-STEM image of a different 2SVL with a Cr@Mo incorporated. (f) ADF and EELS map (570–590 eV) of the boxed region in (e). (g) High resolution ADF-STEM image of the boxed region in (e). White arrows indicate single S atoms either side of the Cr@Mo. Images acquired at 60 kV accelerating voltage and at 300 °C.

experimental TEM data (see Figure S1), it is not possible to discriminate between the S@Mo and Cr@Mo from phase contrast AC-TEM imaging alone.

During imaging, line defects form in MoS<sub>2</sub> due to the sputtering of S atoms by electron beam irradiation.<sup>52</sup> The vacancy production rate is higher at 80 kV than 60 kV. The single S vacancies migrate and aggregate with time to form line defects consisting of a chain of single S vacancies.<sup>59</sup> We found that the Cr@Mo substitutions were also incorporated into these S vacancy lines (SVL), as shown in Figures 4 and 5. Figure 4 shows a time series of room temperature ADF-STEM images acquired at 80 kV of a region containing a impurity atom in a Mo site. As time progresses, more S vacancies are produced, but the location of the substitutional atom remains constant over the 5 min period.

This stability is maintained under elevated temperature, with Figure 5 showing ADF-STEM data acquired at 300 °C. Figure 5a shows a 2SVL (perspective model Figure 5d) containing a Cr@Mo substitution within the SVL, as confirmed by an ADF-STEM imaging with simultaneous EELS mapping over the indicated area (Figure 5b,c). The S vacancies can be identified within the SVL, with the single S atoms indicated with white arrows in Figure 5a. These show “type 1” SVL behavior,<sup>59</sup> where the S atoms lie along a common straight line with the neighboring Mo atoms within the SVL, as opposed to the higher strain, corrugated “type 2” case. Introduction of a Cr@Mo substitution into the Mo–S line of the SVL (Figure 5e,f) does not disturb this type 1 behavior, as can be seen in the high resolution ADF image in Figure 5g. The single S atoms (white

arrows) can be seen to occupy equivalent positions to that expected for Mo, suggesting that the Cr@Mo defect is well incorporated into the defective lattice, likely due to the equivalent valence electron configurations of Mo and Cr.

The metal substitutions were observed to be stable over time at high temperature of 300 °C, only moving when a large number of S atoms are sputtered in their vicinity. Their stability is illustrated in the ADF-STEM time series in Figure 6, showing three substitutions close to one another. Despite the formation of a SVL over the course of imaging the substitutions remain in the same positions with respect to one another, with the left most substitution finally ejected from the lattice in Figure 6d after 5 min 11 s. Increasing the temperature further, to 800 °C, we found that the metal substitutional dopants remained stable (Figure 6e–g). This indicates that dopants incorporated into the MoS<sub>2</sub> lattice during growth temperatures of 700–800 °C will remain incorporated in the lattice.

Density functional theory (DFT) calculations were employed in order to confirm the energetic favorability of substitutional defects, the charge state of the dopant, and the potential change to the electronic properties of the MoS<sub>2</sub> incurred through the single atom doping. Formation energies for both Cr (Figures 7a and b) and V (Figures 7c and d) substitutions for Mo were calculated for a selection of charge states under both Mo-rich (high S vacancy concentration) and S-rich local environments. For Cr@Mo, these yield formation energies of 0.75 eV (Mo rich) and –1.85 eV (S rich). The calculations reveal that the Cr dopant must be an electronically neutral defect, as this is the only stable configuration. Cr possesses the same number of

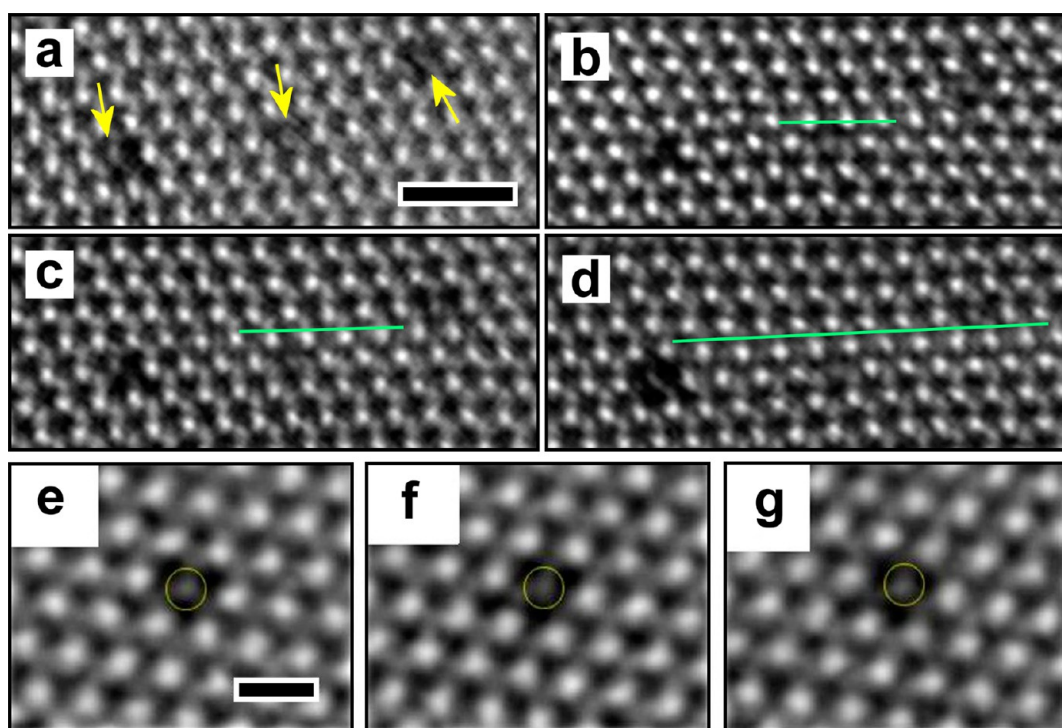


**Figure 6.** High temperature stability of metal substitutional atoms in MoS<sub>2</sub>. (a–d) ADF-STEM time series of three immobile substitutions at 300 °C. Substitution sites indicated with yellow arrows ( $t = 0$  s, 57 s, 3 min 14 s, and 5 min 11 s, respectively). A SVL forms from (b) to (d), indicated by the green line annotation. The left most substitution is ejected in (d). Scale bar 1 nm. (e–f) ADF-STEM time series of images of a metal substitutional dopant remaining fixed at 800 °C ( $t = 0$  s, 1 min 20 s, and 1 min 47 s, respectively). Scale bar 0.5 nm. Beam accelerating voltage at 60 kV.

valence electrons as Mo and so can be expected to form similar chemical bonds with the neighboring S atoms and thus remain electronically neutral. This contrasts with V dopants, which are found to also exhibit stable  $-1$  charge states, suggesting that they may act as a deep single donor in monolayer MoS<sub>2</sub>, with a (0/–) transition level at 0.54 eV above the valence band maximum (VBM). The difference in formation energies is found to be 0.19 eV, with the formation energy of V@Mo corresponding to 0.35 eV (Mo-rich) and 0.04 eV (V-rich). From the formation energy curves in Figure 7c,d, the corresponding Fermi energy is 0.69 eV above valence band maximum (VBM) for Mo-rich condition and 0.91 eV above VBM for S-rich condition. Therefore, our observed V@Mo in experiment is expected to be 1-charged state from our calculation. The electronic density of states (DOS) of Cr@Mo and V@Mo were calculated for the charge neutral states, and also for the  $-1$  charge state for the case of V, shown in Figure 7e–h. The charge neutral Cr@Mo, Figure 7f, shows a new low energy peak in the DOS compared to that of pristine MoS<sub>2</sub>, Figure 7e, indicating doping of the MoS<sub>2</sub> by the presence of the Cr. Neutral V@Mo exhibits a local magnetic moment of  $1 \mu_B$  generated by the V dopant and its bonding with its neighbor S atoms, yielding a state in the band gap, in agreement with previous calculations.<sup>28</sup> However, the DOS for  $-1$  charged V shows no moment due to the filling of the unpaired valence electrons. The DOS of the  $-1$  charged V@Mo, Figure 7h, also shows new low energy peak compared to pristine MoS<sub>2</sub> DOS, confirming it can dope the material.

The evidence suggests that the Cr (and V) substitutions form during CVD growth. The presence of dopants in samples imaged at room temperature strongly supports their intrinsic existence. The metal atoms are in the form of Mo substitutions,

rather than as adatoms positioned on the MoS<sub>2</sub> surface (such as Cr+Mo@Mo),<sup>30</sup> which are more likely to be included during the material growth at high temperature during the synthesis and hard to create at room temperature. The formation of Cr@Mo post-growth would require the ejection of Mo atoms prior to Cr addition and evidence for Mo ejection would be expected; however, no Mo vacancies were apparent in the ADF-STEM or TEM data when imaging under the same conditions. Electron beam induced damage under these imaging conditions was limited to sputtering of S atoms. The source of the Cr and V is most likely from the MoO<sub>3</sub> precursor used in the CVD synthesis, which has been shown in the literature to contain significant trace levels of Cr and V impurities by mass spectroscopy,<sup>60</sup> and atomic absorption spectroscopy.<sup>61</sup>

## CONCLUSION

The presence of single atom substitutions of Cr and V for Mo in CVD monolayer MoS<sub>2</sub> has been experimentally demonstrated by a combination of ADF-STEM and EELS mapping. The substitutions were found to exhibit contrast similar to that expected from a 2S@Mo antisite from ADF-STEM image simulations, highlighting the importance of EELS mapping for the confident identification and delineation between various different possible dopants and self-interstitials. Imaging of Cr@Mo in S vacancy line defects and time-series images at temperatures up to 800 °C confirm that the Cr@Mo substitution is a stable dopant configuration. This information may help in the understanding of the n-type doping commonly seen in TMD materials, which leads to trion emission in the photoluminescence spectra, and the presence of scattering centers in CVD grown TMD monolayers. We hope these

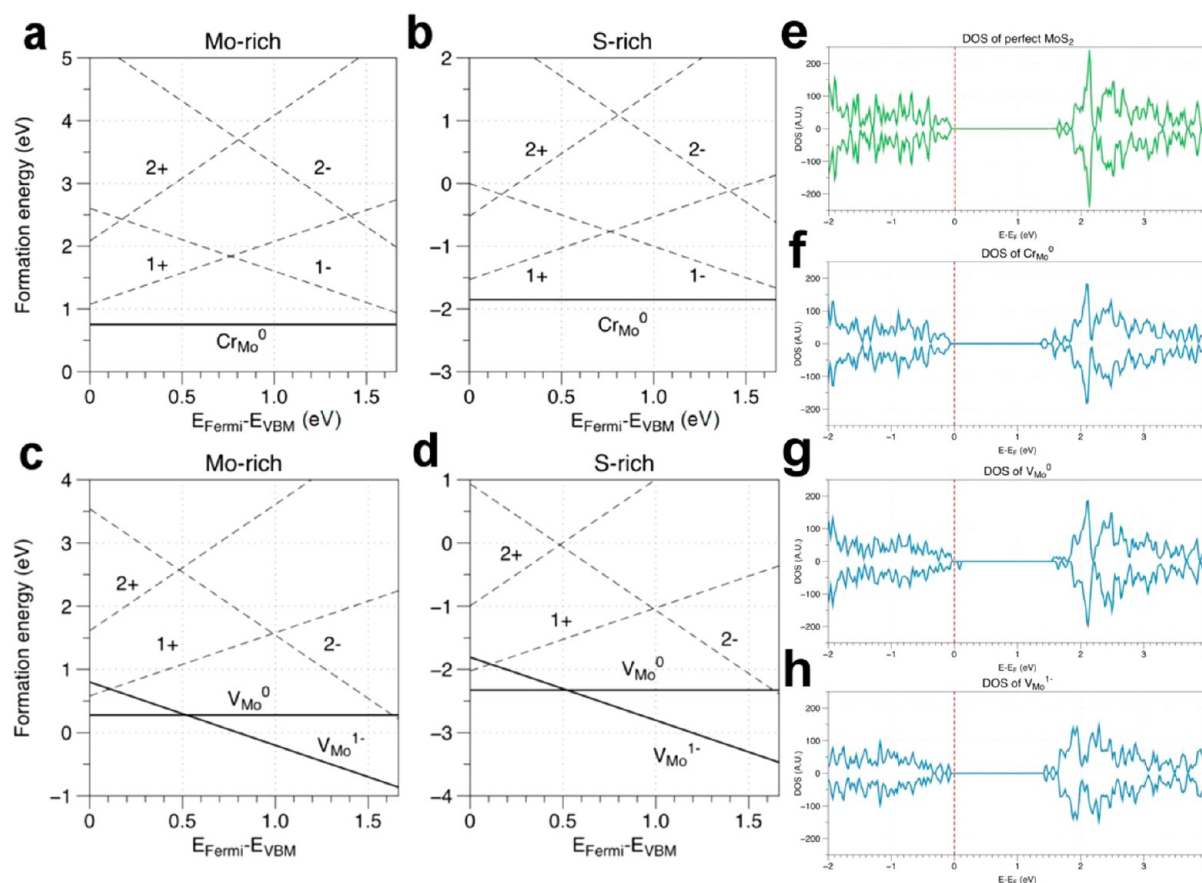


**Figure 7.** Density functional theory (DFT) calculated formation energies and electronic density of states (DOS) of Cr@Mo and V@Mo. (a,b) Formation energies for an isolated Cr@Mo (or  $\text{Cr}_{\text{Mo}}$ ) substitution in  $\text{MoS}_2$ . (c,d) Formation energies for isolated V@Mo. Formation energies for various charge states as a function of the Fermi level inside the band gap are shown. Stable charge states are shown as solid lines. VBM = valence band maximum. (e–h) Electronic density of states calculated by DFT for (e) pristine  $\text{MoS}_2$ , (f) neutral Cr and (g) V substituted  $\text{MoS}_2$ , and (h)  $-1$  charged V substituted  $\text{MoS}_2$ . Fermi level is set to zero and indicated by the dashed line.

results will also be useful in understanding the role of metal dopants in  $\text{MoS}_2$  for work exploring the use of Cr addition as a means of improving the antiwear properties of  $\text{MoS}_2$  solid lubricants.<sup>62</sup>

## METHODS

**Sample Synthesis and Transfer.** Growth of  $\text{MoS}_2$  monolayers on to Si/SiO<sub>2</sub> substrates was achieved using a hydrogen-free atmospheric pressure CVD method, using sulfur (99.5%, Sigma-Aldrich) and  $\text{MoO}_3$  (99.5%, Sigma-Aldrich) precursor powders. The  $\text{MoO}_3$  precursor was initially loaded in a 1 cm diameter tube, which was in turn placed inside a larger diameter 1 in. tube of the CVD furnace. This was in order to prevent cross-contamination of S and  $\text{MoO}_3$  prior to  $\text{MoS}_2$  formation on the target substrate, with the S kept separate in the larger diameter outer tube. Complete details of the dual-tube process, along with schematics, are presented in a previous work.<sup>56</sup> Two furnaces were used to control the temperature of each precursor and the substrate, with heating temperatures of S at 180 °C,  $\text{MoO}_3$  at 300 °C, and the substrate at 800 °C. Ar was used as a carrier gas. The S was left to vaporize for an initial 15 min, before the second furnace was increased to 800 °C at 40 °C/min and left for 15 min under Ar flow of 150 sccm. Ar flow was then reduced to 10 sccm for 25 min, followed by a fast cooling process (sample removal). S temperature was kept at 180 °C throughout.

Transfer of the  $\text{MoS}_2$  was achieved by a commonly used PMMA scaffold technique. A8 950k PMMA was spin-coated (4500 rpm for 60 s) on to the exposed  $\text{MoS}_2$  surface. This was suspended in a 1 mol/L KOH solution to etch away the SiO<sub>2</sub> beneath the  $\text{MoS}_2$ , detaching the  $\text{MoS}_2$ /PMMA film from the substrate. This was then washing in fresh

DI water several times and the film subsequently transferred from the water to a TEM grid—a supported 200 nm thick  $\text{Si}_3\text{N}_4$  film perforated by an array of 2  $\mu\text{m}$  diameter viewing holes (Agar Scientific Y5358). This was air-dried overnight and then baked at 180 °C for 15 min to ensure strong and even adhesion of the film to the grid. The PMMA was then removed by submerging in acetone for 8 h. A similar process is used to transfer the  $\text{MoS}_2$  onto DENS heating holder chips, which contain suspended  $\text{Si}_3\text{N}_4$  membranes with windows cut out by FIB.

**Imaging and Image Processing.** Room temperature ADF-STEM imaging was performed on an aberration corrected JEOL ARM300CF STEM equipped with a JEOL ETA corrector<sup>63</sup> operated at an accelerating voltage of 80 kV (Figures 1 and 4), and 60 kV (Figure 6e–g) located in the electron Physical Sciences Imaging Centre (ePSIC) at Diamond Light Source. Dwell times of 5–20  $\mu\text{s}$  and a pixel size of 0.006 nm px<sup>-1</sup> were used for imaging. Conditions for 60 kV were a CL aperture of 30  $\mu\text{m}$ , convergence semiangle of 31.5 mrad, beam current of 44 pA, and inner acquisition angle of 49.5–198 mrad. For 80 kV a CL aperture of 30  $\mu\text{m}$ , convergence semiangle of 24.6 mrad, beam current of 23 pA, and inner acquisition angle of 39–156 mrad.

High temperature ADF-STEM imaging at 800 °C (Figures 6e–g) was performed using a commercially available *in situ* heating holder from DENS Solutions (SH30-4M-FS) within the JEOL ARM300 STEM. In the DENS Solutions holder, heating the sample was achieved by passing a current through a platinum resistive coil imbedded in the TEM chip (DENS Solutions DENS-C-30). The resistance of the platinum coil is monitored in a four-point configuration, and the temperature is calculated using the Callendar–Van Dusen equation (with calibration constants provided by

the manufacturer). Slits were produced into the Si<sub>3</sub>N<sub>4</sub> membranes using focused ion beam milling.

ADF-STEM imaging and EELS at 300 °C temperature (Figures 2, 3c,e,f, 5, and 6a–d) were conducted on an aberration corrected JEOL-2100F based at AIST, equipped with a DELTA corrector at 60 kV along with a JEOL heating holder for the *in situ* temperature control. A convergence semiangle of 35 mrad and inner acquisition semiangle of 79 mrad were used. The beam current was approximately 10 pA. A dwell time of ~30–40 μs was used, with a pixel size of ~0.005 to 0.013 nm px<sup>-1</sup>. Total dose per image was therefore ~10<sup>8</sup> e nm<sup>-2</sup>.

AC-TEM (Figure 3i) was performed on a JEOL 2200MCO at Oxford, with a CEOS corrector at 80 kV at room temperature. Beam current density under imaging conditions was ~10<sup>5</sup> e nm<sup>-2</sup> s<sup>-1</sup> with typical exposure times of 1–3 s.

(S)TEM images in Figures 1, 2, 3, and 6 were subjected to a Gaussian smooth. An intensity and position preserving Savitsky–Golay spatial filter was used to smooth the images in Figures 5a and e, to preserve the relatively weak S signal in the SVL.

EELS data was processed using the Cornell Spectrum Imager plugin for ImageJ.<sup>64</sup> An exponential was fitted along the region 50–100 eV before the peaks of interest for background subtraction. No further (e.g., Hartree–Slater) subtraction was performed. The EELS mapping images correspond to the relative integrated EELS intensity; this area is integrated between the stated energies (typically integrated between 505 and 525 eV for V and 570–590 eV for Cr L peaks). This integrated intensity is acquired after background subtraction.

**Image Simulations.** Both TEM and ADF image simulations were performed using JEMS software.<sup>65</sup> TEM simulations were done in the HR-TEM multislice portion of the package, using 80 kV accelerating voltage, 6 nm defocus spread, 3 nm defocus, and C<sub>s</sub> = 5 μm. ADF simulations were performed using the HAADF image simulation component, with 4 nm defocus, 5.3 nm defocus spread, 60 kV accelerating voltage, C<sub>c</sub> = 1.2 mm, energy spread of 0.80 eV, C<sub>s</sub> = 2 μm, 0 nm 2-fold astigmatism, 37 nm (57°) 3-fold astigmatism, 30 nm coma (115°), 35 mrad half convergence angle, and using Weickenmeier–Kohn atomic form factors with core and phonon absorption with 600 K frozen phonons. Brightness and contrast of the simulated images were adjusted such that the intensities of known atomic columns (1 × Mo, 2 × S, and 1 × S) were in agreement with experiment (Figure 3d, black plot).

**Density Functional Theory.** DFT calculations are carried out to calculate formation energies of the charged dopants Cr@Mo and V@Mo. The calculations are performed within the generalized gradient approximation (GGA) of the Perdew–Burke–Ernzerhof (PBE) functional<sup>66</sup> using Vienna *ab initio* simulation package (VASP) code.<sup>67</sup> In the calculation, the basis set contains plane waves up to an energy cutoff of 350 eV, and the structure is relaxed until the force on each atom is smaller than 0.02 eV/Å. The 2 × 2 × 1 grid for k-point is used for the supercell calculations. The in-plane lattice constant of the monolayer MoS<sub>2</sub> is calculated to be *a* = 3.191 Å and we used this lattice constant as a basic unit length in all directions for the supercell calculations. The formation energies of the charged defects in neutral and charged states are calculated.

The formula of the formation energy is

$$E_{\text{form}} = E_{\text{total}}^{\text{defect}} - E_{\text{total}}^{\text{perfect}} + \mu_{\text{Mo}} - \mu_{\text{X}} + q(E_{\text{VBM}}^{\text{perfect}} + E_{\text{Fermi}}) + E_{\text{corr}} \quad (1)$$

where  $E_{\text{total}}^{\text{defect}}$  is the total energy of a monolayer MoS<sub>2</sub> containing Cr (or V) dopants in the  $a(6 \times 6 \times 6)$  supercell and  $E_{\text{total}}^{\text{perfect}}$  is the total energy of a perfect MoS<sub>2</sub> supercell without a defect.  $\mu_{\text{Mo}}$  is the chemical potential of the Mo and  $\mu_{\text{X}}$  is the chemical potential of the X = Cr, V. These chemical potentials are determined separately in the Mo-rich and the S-rich conditions. In the Mo-rich condition,  $\mu_{\text{Mo}}$  is determined by calculation of the total energy of bulk (bcc) Mo. In the S-rich condition,  $\mu_{\text{Mo}}$  is determined from  $\mu_{\text{MoS}_2}$ , that is, total energy of the primitive MoS<sub>2</sub> monolayer and  $\mu_{\text{S}}$  that determined by total energy of the S orthorhombic crystal. To determine chemical potential of a Cr and V, chemical potentials of all the experimentally known stable

binary phases of Cr (or V) and S are calculated because it is hard to directly discern present stable binary phase in the experiments.<sup>68,69</sup> Chemical potentials of the CrS, Cr<sub>7</sub>S<sub>8</sub>, Cr<sub>5</sub>S<sub>6</sub>, Cr<sub>3</sub>S<sub>4</sub>, Cr<sub>2</sub>S<sub>3</sub>, and Cr<sub>5</sub>S<sub>8</sub> (VS<sub>4</sub>, V<sub>3</sub>S<sub>4</sub>, V<sub>5</sub>S<sub>8</sub>, V<sub>5</sub>S<sub>4</sub>, and V<sub>3</sub>S for the V–S binary phase) are calculated and the lowest value of  $\mu_{\text{Cr}}$  ( $\mu_{\text{V}}$ ) that can be considered as the most stable phases is selected among each cases. *q* is the charge state of the defect,  $E_{\text{VBM}}^{\text{perfect}}$  is the valence band maximum (VBM) of a monolayer MoS<sub>2</sub> without a defect, and  $E_{\text{Fermi}}$  is the Fermi level with the reference to the  $E_{\text{VBM}}^{\text{perfect}}$ .  $E_{\text{corr}}$  is the energy correction term including the potential alignment and the compensation to the artificial electrostatic energy induced by image charges in supercells for charged defects. The detail explanation of the calculation of  $E_{\text{corr}}$  is described in somewhere.<sup>70,71</sup>

## ASSOCIATED CONTENT

### Supporting Information

The Supporting Information is available free of charge on the ACS Publications website at DOI: 10.1021/acsnano.6b05674.

AC-TEM image of monolayer CVD MoS<sub>2</sub> with intensity line profiles. (PDF)

## AUTHOR INFORMATION

### Corresponding Authors

\*E-mail: alex.robertson2@materials.ox.ac.uk.

\*E-mail: jamie.warner@materials.ox.ac.uk.

### Notes

The authors declare no competing financial interest.

## ACKNOWLEDGMENTS

J.H.W. thanks the support from the Royal Society. A.W.R. has been supported by EPSRC (Platform Grant EP/K032518/1) and KIER (B6-2452). G.-D.L. and E.Y. acknowledge support from the Supercomputing Center/Korea Institute of Science and Technology Information with supercomputing resources (KSC-2013-C3-058), from the BK21 plus program, and from the National Research Foundation of Korea (NRF) grant funded by the Korea government (RIAM No. 2010-0012670, MSIP No. 2013003535). Y.C.L. and K.S. acknowledge the support from JST ACCEL. This work was conducted under framework of the research and development program of the Korea Institute of Energy Research (B6-2452). A.I.K. acknowledges EPSRC support under platform grant EP/K032518/1.

## REFERENCES

- (1) Mak, K. F.; Lee, C.; Hone, J.; Shan, J.; Heinz, T. F. Atomically Thin MoS<sub>2</sub>: A New Direct-Gap Semiconductor. *Phys. Rev. Lett.* **2010**, *105*, 136805.
- (2) Hansen, L. P.; Ramasse, Q. M.; Kisielowski, C.; Brorson, M.; Johnson, E.; Topsøe, H.; Helveg, S. Atomic-Scale Edge Structures on Industrial-Style MoS<sub>2</sub> Nanocatalysts. *Angew. Chem., Int. Ed.* **2011**, *50*, 10153–10156.
- (3) Jaramillo, T. F.; Jørgensen, K. P.; Bonde, J.; Nielsen, J. H.; Horch, S.; Chorkendorff, I. Identification of Active Edge Sites for Electrochemical H<sub>2</sub> Evolution from MoS<sub>2</sub> Nanocatalysts. *Science* **2007**, *317*, 100–102.
- (4) Le, D.; Rawal, T. B.; Rahman, T. S. Single-Layer MoS<sub>2</sub> with Sulfur Vacancies: Structure and Catalytic Application. *J. Phys. Chem. C* **2014**, *118*, 5346–5351.
- (5) Yin, Z.; Li, H.; Li, H.; Jiang, L.; Shi, Y.; Sun, Y.; Lu, G.; Zhang, Q.; Chen, X.; Zhang, H. Single-Layer MoS<sub>2</sub> Phototransistors. *ACS Nano* **2012**, *6*, 74–80.
- (6) Britnell, L.; Ribeiro, R. M.; Eckmann, A.; Jalil, R.; Belle, B. D.; Mishchenko, A.; Kim, Y.-J.; Gorbachev, R. V.; Georgiou, T.; Morozov, S. V.; Grigorenko, A. N.; Geim, A. K.; Casiraghi, C.; Castro Neto, A.

H.; Novoselov, K. S. Strong Light-Matter Interactions in Heterostructures of Atomically Thin Films. *Science* **2013**, *340*, 1311–1314.

(7) Gong, Y.; Lin, J.; Wang, X.; Shi, G.; Lei, S.; Lin, Z.; Zou, X.; Ye, G.; Vajtai, R.; Yakobson, B. I.; Terrones, H.; Tay, B. K.; Lou, J.; Pantelides, S. T.; Liu, Z.; Zhou, W.; Ajayan, P. M.; Terrones, M. Vertical and in-Plane Heterostructures from WS<sub>2</sub>/MoS<sub>2</sub> Monolayers. *Nat. Mater.* **2014**, *13*, 1135–1142.

(8) Nicolosi, V.; Chhowalla, M.; Kanatzidis, M. G.; Strano, M. S.; Coleman, J. N. Liquid Exfoliation of Layered Materials. *Science* **2013**, *340*, 1226419.

(9) Coleman, J. N.; Lotya, M.; O'Neill, A.; Bergin, S. D.; King, P. J.; Khan, U.; Young, K.; Gaucher, A.; De, S.; Smith, R. J.; Shvets, I. V.; Arora, S. K.; Stanton, G.; Kim, H. - Y.; Lee, K.; Kim, G. T.; Duesberg, G. S.; Hallam, T.; Boland, J. J.; Wang, J. J.; et al. Two-Dimensional Nanosheets Produced by Liquid Exfoliation of Layered Materials. *Science* **2011**, *331*, 568–571.

(10) Wang, X.; Feng, H.; Wu, Y.; Jiao, L. Controlled Synthesis of Highly Crystalline MoS<sub>2</sub> Flakes by Chemical Vapor Deposition. *J. Am. Chem. Soc.* **2013**, *135*, 5304–5307.

(11) Lee, Y.; Zhang, X.-Q.; Zhang, W.; Chang, M.-T.; Lin, C.-T.; Chang, K.-D.; Yu, Y.; Wang, J. T.; Chang, C.; Li, L.; Lin, T. - W. Synthesis of Large-Area MoS<sub>2</sub> Atomic Layers with Chemical Vapor Deposition. *Adv. Mater.* **2012**, *24*, 2320–2325.

(12) Najmaei, S.; Liu, Z.; Zhou, W.; Zou, X.; Shi, G.; Lei, S.; Yakobson, B. I.; Idrobo, J.-C.; Ajayan, P. M.; Lou, J. Vapour Phase Growth and Grain Boundary Structure of Molybdenum Disulfide Atomic Layers. *Nat. Mater.* **2013**, *12*, 754–759.

(13) Kang, K.; Xie, S.; Huang, L.; Han, Y.; Huang, P. Y.; Mak, K. F.; Kim, C.-J.; Muller, D.; Park, J. High-Mobility Three-Atom-Thick Semiconducting Films with Wafer-Scale Homogeneity. *Nature* **2015**, *520*, 656–660.

(14) Radisavljevic, B.; Radenovic, A.; Brivio, J.; Giacometti, V.; Kis, A. Single-Layer MoS<sub>2</sub> Transistors. *Nat. Nanotechnol.* **2011**, *6*, 147–150.

(15) Tedstone, A. A.; Lewis, D. J.; O'Brien, P. Synthesis, Properties, and Applications of Transition Metal-Doped Layered Transition Metal Dichalcogenides. *Chem. Mater.* **2016**, *28*, 1965–1974.

(16) Du, Y.; Liu, H.; Neal, A. T.; Si, M.; Ye, P. D. Molecular Doping of Multilayer MoS<sub>2</sub> Field-Effect Transistors: Reduction in Sheet and Contact Resistances. *IEEE Electron Device Lett.* **2013**, *34*, 1328–1330.

(17) McDonnell, S.; Addou, R.; Buie, C.; Wallace, R. M.; Hinkle, C. L. Defect-Dominated Doping and Contact Resistance in MoS<sub>2</sub>. *ACS Nano* **2014**, *8*, 2880–2888.

(18) Liu, D.; Guo, Y.; Fang, L.; Robertson, J. Sulfur Vacancies in Monolayer MoS<sub>2</sub> and Its Electrical Contacts. *Appl. Phys. Lett.* **2013**, *103*, 183113.

(19) Das, S.; Chen, H. Y.; Penumatcha, A. V.; Appenzeller, J. High Performance Multilayer MoS<sub>2</sub> Transistors with Scandium Contacts. *Nano Lett.* **2013**, *13*, 100–105.

(20) Walia, S.; Balendhran, S.; Wang, Y.; Ab Kadir, R.; Sabirin Zoofakar, A.; Atkin, P.; Zhen Ou, J.; Sriram, S.; Kalantar-Zadeh, K.; Bhaskaran, M. Characterization of Metal Contacts for Two-Dimensional MoS<sub>2</sub> Nanoflakes. *Appl. Phys. Lett.* **2013**, *103*, 232105.

(21) Du, Y.; Yang, L.; Liu, H.; Ye, P. D. Contact Research Strategy for Emerging Molybdenum Disulfide and Other Two-Dimensional Field-Effect Transistors. *APL Mater.* **2014**, *2*, 092510.

(22) Addou, R.; McDonnell, S.; Barrera, D.; Guo, Z.; Azcatl, A.; Wang, J.; Zhu, H.; Hinkle, C. L.; Quevedo-Lopez, M.; Alshareef, H. N.; Colombo, L.; Hsu, J. W. P.; Wallace, R. M. Impurities and Electronic Property Variations of Natural MoS<sub>2</sub> Crystal Surfaces. *ACS Nano* **2015**, *9*, 9124–9133.

(23) Zhu, W.; Low, T.; Lee, Y. H.; Wang, H.; Farmer, D. B.; Kong, J.; Xia, F.; Avouris, P. Electronic Transport and Device Prospects of Monolayer Molybdenum Disulfide Grown by Chemical Vapour Deposition. *Nat. Commun.* **2014**, *5*, 3087.

(24) Durand, C.; Zhang, X.; Fowlkes, J.; Najmaei, S.; Lou, J.; Li, A.-P. Defect-Mediated Transport and Electronic Irradiation Effect in Individual Domains of CVD-Grown Monolayer MoS<sub>2</sub>. *J. Vac. Sci. Technol. B* **2015**, *33*, 02B110.

(25) Zafar, A.; Nan, H.; Zafar, Z.; Wu, Z.; Jiang, J.; You, Y.; Ni, Z. Probing the Intrinsic Optical Quality of CVD Grown MoS<sub>2</sub>. **2016**, *arXiv:1609.09307*. arXiv.org e-Print archive. <http://arxiv.org/abs/1609.09307> (accessed September, 2016).

(26) Ganatra, R.; Zhang, Q. Few-Layer MoS<sub>2</sub>: A Promising Layered Semiconductor. *ACS Nano* **2014**, *8*, 4074–4099.

(27) Noh, J.-Y.; Kim, H.; Kim, Y.-S. Stability and Electronic Structures of Native Defects in Single-Layer MoS<sub>2</sub>. *Phys. Rev. B: Condens. Matter Mater. Phys.* **2014**, *89*, 205417.

(28) Yue, Q.; Chang, S.; Qin, S.; Li, J. Functionalization of Monolayer MoS<sub>2</sub> by Substitutional Doping: A First-Principles Study. *Phys. Lett. A* **2013**, *377*, 1362–1367.

(29) Dolui, K.; Rungger, I.; Das Pemmaraju, C.; Sanvito, S. Possible Doping Strategies for MoS<sub>2</sub> Monolayers: An *Ab Initio* Study. *Phys. Rev. B: Condens. Matter Mater. Phys.* **2013**, *88*, 075420.

(30) Lin, Y. C.; Dumcenco, D. O.; Komsa, H. P.; Niimi, Y.; Krasheninnikov, A. V.; Huang, Y. S.; Suenaga, K. Properties of Individual Dopant Atoms in Single-Layer MoS<sub>2</sub>: Atomic Structure, Migration, and Enhanced Reactivity. *Adv. Mater.* **2014**, *26*, 2857–2861.

(31) Zhou, W.; Zou, X.; Najmaei, S.; Liu, Z.; Shi, Y.; Kong, J.; Lou, J.; Ajayan, P. M.; Yakobson, B. I.; Idrobo, J.-C. Intrinsic Structural Defects in Monolayer Molybdenum Disulfide. *Nano Lett.* **2013**, *13*, 2615–2622.

(32) Komsa, H.-P.; Kotakoski, J.; Kurasch, S.; Lehtinen, O.; Kaiser, U.; Krasheninnikov, A. V. Two-Dimensional Transition Metal Dichalcogenides under Electron Irradiation: Defect Production and Doping. *Phys. Rev. Lett.* **2012**, *109*, 035503.

(33) Hong, J.; Hu, Z.; Probert, M.; Li, K.; Lv, D.; Yang, X.; Gu, L.; Mao, N.; Feng, Q.; Xie, L.; Zhang, J.; Wu, D.; Zhang, Z.; Jin, C.; Ji, W.; Zhang, X.; Yuan, J.; Zhang, Z. Exploring Atomic Defects in Molybdenum Disulfide Monolayers. *Nat. Commun.* **2015**, *6*, 6293.

(34) Lahiri, J.; Lin, Y.; Bozkurt, P.; Oleynik, I. I.; Batzill, M. An Extended Defect in Graphene as a Metallic Wire. *Nat. Nanotechnol.* **2010**, *5*, 326–9.

(35) Ma, C.; Sun, H.; Zhao, Y.; Li, B.; Li, Q.; Zhao, A.; Wang, X.; Luo, Y.; Yang, J.; Wang, B.; Hou, J. G. Evidence of van Hove Singularities in Ordered Grain Boundaries of Graphene. *Phys. Rev. Lett.* **2014**, *112*, 226802.

(36) Sun, L.; Banhart, F.; Warner, J. Two-Dimensional Materials under Electron Irradiation. *MRS Bull.* **2015**, *40*, 29–37.

(37) Robertson, A. W.; Warner, J. H. Atomic Resolution Imaging of Graphene by Transmission Electron Microscopy. *Nanoscale* **2013**, *5*, 4079–4093.

(38) Wang, Q. H.; Kalantar-Zadeh, K.; Kis, A.; Coleman, J. N.; Strano, M. S. Electronics and Optoelectronics of Two-Dimensional Transition Metal Dichalcogenides. *Nat. Nanotechnol.* **2012**, *7*, 699–712.

(39) He, Z.; Xu, W.; Zhou, Y.; Wang, X.; Sheng, Y.; Rong, Y.; Guo, S.; Zhang, J.; Smith, J. M.; Warner, J. H. Biexciton Formation in Bilayer Tungsten Disulfide. *ACS Nano* **2016**, *10*, 2176–2183.

(40) Lei, S.; Ge, L.; Najmaei, S.; George, A.; Kappera, R.; Lou, J.; Chhowalla, M.; Yamaguchi, H.; Gupta, G.; Vajtai, R.; Mohite, A. D.; Ajayan, P. M. Evolution of the Electronic Band Structure and Efficient Photo-Detection in Atomic Layers of InSe. *ACS Nano* **2014**, *8*, 1263–1272.

(41) Cohen-Tanugi, D.; Grossman, J. C. Nanoporous Graphene as a Reverse Osmosis Membrane: Recent Insights from Theory and Simulation. *Desalination* **2015**, *366*, 59–70.

(42) Robertson, A. W.; Lee, G.; He, K.; Gong, C.; Chen, Q.; Yoon, E.; Kirkland, A. I.; Warner, J. H. Atomic Structure of Graphene Subnanometer Pores. *ACS Nano* **2015**, *9*, 11599–11607.

(43) Robertson, A. W.; Lee, G.-D.; He, K.; Yoon, E.; Kirkland, A. I.; Warner, J. H. The Role of the Bridging Atom in Stabilizing Odd Numbered Graphene Vacancies. *Nano Lett.* **2014**, *14*, 3972–3980.

(44) Warner, J. H.; Margine, E. R.; Mukai, M.; Robertson, A. W.; Giustino, F.; Kirkland, A. I. Dislocation-Driven Deformations in Graphene. *Science* **2012**, *337*, 209–212.

- (45) Tsen, A. W.; Brown, L.; Levendorf, M. P.; Ghahari, F.; Huang, P. Y.; Havener, R. W.; Ruiz-Vargas, C. S.; Muller, D. A.; Kim, P.; Park, J. Tailoring Electrical Transport across Grain Boundaries in Polycrystalline Graphene. *Science* **2012**, *336*, 1143–1146.
- (46) Suenaga, K.; Koshino, M. Atom-by-Atom Spectroscopy at Graphene Edge. *Nature* **2010**, *468*, 1088–1090.
- (47) Kurasch, S.; Kotakoski, J.; Lehtinen, O.; Skákalová, V.; Smet, J.; Krill, C. E.; Krasheninnikov, A. V.; Kaiser, U. Atom-by-Atom Observation of Grain Boundary Migration in Graphene. *Nano Lett.* **2012**, *12*, 3168–3173.
- (48) Robertson, A. W.; Lee, G.-D.; He, K.; Fan, Y.; Allen, C. S.; Lee, S.; Kim, H.; Yoon, E.; Zheng, H.; Kirkland, A. I.; Warner, J. H. Partial Dislocations in Graphene and Their Atomic Level Migration Dynamics. *Nano Lett.* **2015**, *15*, 5950–5955.
- (49) Meyer, J.; Eder, F.; Kurasch, S.; Skakalova, V.; Kotakoski, J.; Park, H.; Roth, S.; Chuvilin, A.; Eyhusen, S.; Benner, G.; Krasheninnikov, A. V.; Kaiser, U. Accurate Measurement of Electron Beam Induced Displacement Cross Sections for Single-Layer Graphene. *Phys. Rev. Lett.* **2012**, *108*, 196102.
- (50) Robertson, A. W.; Allen, C. S.; Wu, Y. A.; He, K.; Olivier, J.; Neethling, J.; Kirkland, A. I.; Warner, J. H. Spatial Control of Defect Creation in Graphene at the Nanoscale. *Nat. Commun.* **2012**, *3*, 1144.
- (51) Lin, J.; Pantelides, S. T.; Zhou, W. Vacancy-Induced Formation and Growth of Inversion Domains in Transition-Metal Dichalcogenide Monolayer. *ACS Nano* **2015**, *9*, 5189–5197.
- (52) Lin, Y.-C.; Dumcenco, D. O.; Huang, Y.-S.; Suenaga, K. Atomic Mechanism of the Semiconducting-to-Metallic Phase Transition in Single-Layered MoS<sub>2</sub>. *Nat. Nanotechnol.* **2014**, *9*, 391–396.
- (53) Krivanek, O. L.; Chisholm, M. F.; Nicolosi, V.; Pennycook, T. J.; Corbin, G. J.; Dellby, N.; Murfitt, M. F.; Own, C. S.; Szilagy, Z. S.; Oxley, M. P.; Pantelides, S. T.; Pennycook, S. J. Atom-by-Atom Structural and Chemical Analysis by Annular Dark-Field Electron Microscopy. *Nature* **2010**, *464*, 571–574.
- (54) Warner, J. H.; Lin, Y. C.; He, K.; Koshino, M.; Suenaga, K. Stability and Spectroscopy of Single Nitrogen Dopants in Graphene at Elevated Temperatures. *ACS Nano* **2014**, *8*, 11806–11815.
- (55) Lin, Y.-C.; Teng, P.-Y.; Yeh, C.-H.; Koshino, M.; Chiu, P.-W.; Suenaga, K. Structural and Chemical Dynamics of Pyridinic-Nitrogen Defects in Graphene. *Nano Lett.* **2015**, *15*, 7408–7413.
- (56) Wang, S.; Pacios, M.; Bhaskaran, H.; Warner, J. H. Substrate Control for Large Area Continuous Films of Monolayer MoS<sub>2</sub> by Atmospheric Pressure Chemical Vapor Deposition. *Nanotechnology* **2016**, *27*, 085604.
- (57) Krasheninnikov, A.; Lehtinen, P.; Foster, A.; Pyykkö, P.; Nieminen, R. Embedding Transition-Metal Atoms in Graphene: Structure, Bonding, and Magnetism. *Phys. Rev. Lett.* **2009**, *102*, 126807.
- (58) Robertson, A. W.; Montanari, B.; He, K.; Kim, J.; Allen, C. S.; Wu, Y. A.; Olivier, J.; Neethling, J.; Harrison, N.; Kirkland, A. I.; Warner, J. H. Dynamics of Single Fe Atoms in Graphene Vacancies. *Nano Lett.* **2013**, *13*, 1468–1475.
- (59) Wang, S.; Lee, G.-D.; Lee, S.; Yoon, E.; Warner, J. H. Detailed Atomic Reconstruction of Extended Line Defects in Monolayer MoS<sub>2</sub>. *ACS Nano* **2016**, *10*, 5419–5430.
- (60) Khomyakov, A. V.; Mozhevitina, E. N.; Sadovskii, A. P.; Sukharev, V. A.; Avetissov, I. K. Purity of MoO<sub>3</sub> from Different Manufacturers. *Inorg. Mater.* **2016**, *52*, 285–293.
- (61) Parant, J. P.; Villela, G.; Gourier, D.; Le Sergent, C.; Dumas, J. P. Influence of Chromium Content on the Coloration of PbMoO<sub>4</sub> Crystals. *J. Cryst. Growth* **1981**, *52*, 576–579.
- (62) Tedstone, A. A.; Lewis, D. J.; Hao, R.; Mao, S.-M.; Bellon, P.; Averback, R. S.; Warrens, C. P.; West, K. R.; Howard, P.; Gaemers, S.; Dillon, S. J.; O'Brien, P. Mechanical Properties of Molybdenum Disulfide and the Effect of Doping: An *in Situ* TEM Study. *ACS Appl. Mater. Interfaces* **2015**, *7*, 20829–20834.
- (63) Hosokawa, F.; Sawada, H.; Kondo, Y.; Takayanagi, K.; Suenaga, K. Development of Cs and Cc correctors for transmission electron microscopy. *Microscopy* **2013**, *62*, 23–41.
- (64) Cueva, P.; Hovden, R.; Mundy, J. A.; Xin, H. L.; Muller, D. A. Data Processing for Atomic Resolution Electron Energy Loss Spectroscopy. *Microsc. Microanal.* **2012**, *18*, 667–675.
- (65) Stadelmann, P. *Electron Microscopy Simulation Software*, <http://www.jems-saas.ch/>, accessed 11/7/2016.
- (66) Perdew, J. P.; Burke, K.; Ernzerhof, M. Generalized Gradient Approximation Made Simple. *Phys. Rev. Lett.* **1996**, *77*, 3865–3868.
- (67) Kresse, G.; Furthmüller, J. Efficient Iterative Schemes for *Ab Initio* Total-Energy Calculations Using a Plane-Wave Basis Set. *Phys. Rev. B: Condens. Matter Mater. Phys.* **1996**, *54*, 11169–11186.
- (68) Predel, B. *Landolt-Börnstein—Group IV Physical Chemistry*, 5D, 1–6; Springer-Verlag: New York, 1994.
- (69) Predel, B. *Landolt-Börnstein—Group IV Physical Chemistry*, 5J, 1–3; Springer-Verlag: New York, 1998.
- (70) Noh, J.-Y.; Kim, H.; Kim, Y.-S. Stability and Electronic Structures of Native Defects in Single-Layer MoS<sub>2</sub>. *Phys. Rev. B: Condens. Matter Mater. Phys.* **2014**, *89*, 205417.
- (71) Komsa, H.-P.; Pasquarello, A. Finite-Size Supercell Correction for Charged Defects at Surfaces and Interfaces. *Phys. Rev. Lett.* **2013**, *110*, 095505.